Crust Effects on Liquefaction Response: Insights from Centrifuge Tests

Nikolaos Ntritsos[a*]

[a] University of Pavia, Department of Civil Engineering and Architecture, Pavia, Italy,

nikolaos.ntritsos@unipv.it

* Corresponding Author

ABSTRACT

A series of seismic centrifuge tests were performed to investigate how the hydromechanical characteristics of non-liquefiable crusts influence the response of layered liquefiable deposits. Two vertically continuous liquefiable profiles were examined, each overlain by three contrasting crust types: dense coarse sand, lightly overconsolidated silt, and heavily overconsolidated clay. High excess pore pressures developed throughout the liquefiable profiles and sustained upward flow, with crust properties governing how this inflow was accommodated and discharged. In sand-crust models, substantial drainage occurred during shaking, reducing liquefaction severity in the underlying critical layer while enabling early co-seismic settlement. The low-permeability silt and clay crusts promoted fluid accumulation and prolonged liquefaction in the critical layer but produced contrasting surface responses. The silt combined sufficient hydraulic resistance to intensify void redistribution with insufficient mechanical and erosion resistance to maintain crust integrity under cyclic loading and subsequent seepage. Extensive fluidization of the critical layer and breakdown of the silt structure produced large settlement and surface ejecta. The clay largely retained its stiffness and structural integrity, partly decoupling surface movement from underlying sand sedimentation. The findings demonstrate that factors beyond crust thickness, including crust permeability, stiffness, cyclic strength and erodibility, strongly influence liquefaction response and related damage potential.

Keywords: *liquefaction; crust; centrifuge; earthquake; ejecta; settlement*

1. INTRODUCTION

Natural liquefiable deposits are rarely uniform; instead, they typically comprise distinct soil layers with varying physical and behavioural characteristics. The deposit response during earthquake shaking is largely governed by dynamic hydromechanical interactions among these different layers and other system-level effects. Recent case-history observations and nonlinear dynamic analyses demonstrate that such cross-layer interactions of liquefying deposits can profoundly influence the development and severity of the liquefaction response (e.g. Cubrinovski et al. 2019, Bassal et al. 2022, Cubrinovski and Ntritsos, 2023). Thus, the resulting damage reflects the response of the deposit as a system and cannot be inferred solely from liquefaction triggering within an individual (critical) layer.

The surface crust overlying the liquefied soil is a particularly important component in this system of interacting layers. Here, the crust is defined as the uppermost part of the deposit extending from the ground surface to the top of the underlying liquefiable soil. It comprises all soils above the groundwater level and any vertically connected submerged soils that are non-liquefiable because of their high density, plasticity, or other favourable properties. During a strong earthquake, the crust becomes the layer that separates the liquefied subsoil from structures or other installations founded on or near the ground surface. Consequently, its cyclic response and hydromechanical interactions with the underlying layers exert a fundamental influence on the nature and severity of liquefaction effects at the ground surface.

The engineering significance of the non-liquefiable crust has been broadly recognized following the seminal work of Ishihara (1985). Using several post-earthquake observations, Ishihara developed simple criteria identifying conditions for occurrence of liquefaction-induced ground failure based on the thickness of the liquefied layer and thickness of the non-liquefiable crust. Later, Naesgaard et al. (1998) and Bouckovalas and Dakoulas (2007) also

demonstrated the beneficial effect of a thick non-liquefiable crust on the seismic performance of shallow foundations, using nonlinear dynamic analyses. In today's practice, the importance of crust thickness is well-established and commonly used empirical methods for liquefaction damage assessment incorporate its effect, at least implicitly. In contrast, other important hydromechanical properties of the crust remain incompletely represented in these empirical methods.

Previous work has indicated that crust properties, such as permeability, compressibility, shear strength and the overall crust integrity may affect the nature and severity of liquefaction effects at the ground surface (e.g. Yoshimi and Kuwabara, 1973; Scott and Zuckerman, 1973; Fiegel and Kutter, 1994; Obermeier et al. 2005; Hutabarat and Bray, 2022). Much of this work has focused on particular mechanisms, response measures, or damage indicators, while comparatively little evidence exists on how contrasting crust types affect the complete system response, from pore pressure redistribution and deformation within the deposit to settlement and ejecta manifestation at the ground surface. Such crust effects are difficult to isolate from field observations, whereas continuum-based numerical analysis cannot readily capture post-liquefaction sedimentation and important near-surface processes involving cracking, localized erosion, piping and sand-boil formation. In this context, controlled centrifuge modelling is uniquely suited to investigate the influence of crust characteristics on liquefaction response.

This paper investigates the influence of crust characteristics on free-field, level-ground liquefaction response through a series of seismic centrifuge tests. Two vertically continuous liquefiable profiles are examined beneath crusts with contrasting hydromechanical properties. Crust effects on the following key aspects of the liquefaction response are addressed:

- generation, redistribution and dissipation of excess pore pressure (EPP);
- shear-strain development;

- magnitude, timing and uniformity of surface settlement;
- surface manifestation of sand ejecta.

Details of the centrifuge tests and selected results are presented and discussed following a brief background on the system response of vertically continuous liquefiable deposits.

2. SYSTEM RESPONSE OF VERTICALLY CONTINUOUS DEPOSITS

Liquefiable sites commonly comprise irregularly distributed liquefiable and non-liquefiable soils. From a liquefaction consequences viewpoint, the vertical continuity of liquefiable soils is of particular importance, as case histories have shown that soil profiles with thick interconnected liquefiable layers – referred to as vertically continuous (VC) deposits – tend to exhibit more severe liquefaction effects than profiles with interbedded liquefiable and non-liquefiable layers (e.g. Cubrinovski et al. 2019, Dhakal et al. 2026).

Fig. 1 shows typical soil profile characteristics of VC deposits that exhibited severe liquefaction damage during the 2010–2011 Christchurch, New Zealand earthquakes (Cubrinovski and Ntritsos, 2023; Dhakal et al. 2026). These deposits contain vertically continuous liquefiable soils within the upper 10 m and have a shallow groundwater table at approximately 2 m depth. They are typically composed of a shallow critical layer of silty sand or sandy silt, 1–5 m thick, overlying a denser sand. The normalized equivalent clean sand cone resistance, q_{c1Ncs}, is relatively low in the critical layer, at 80–100, and increases gradually with depth through the base sand to approximately 130–150.

The seismic response of such VC deposits has been scrutinized by Cubrinovski et al. (2019) and Cubrinovski and Ntritsos (2023), using nonlinear dynamic effective stress analysis. These studies identified several cascading mechanisms and effects that collectively increase the

severity of liquefaction response in VC deposits. Fig. 1 schematically illustrates a characteristic VC-deposit response scenario, involving the principal mechanisms summarized below.

(1) Liquefaction is initially triggered in the shallow critical layer.

(2) Water subsequently flows into the critical layer from the underlying soils, which may not reach full liquefaction but generate higher EPPs than those in the critical layer. The combined effects of shaking-induced liquefaction and inflow of water from the underlying soils result in severe fluidization of the low-resistance critical layer.

(3) The vertical continuity of the liquefiable soils allows excess water generated throughout the deposit to migrate upward without interception by non-liquefiable interlayers, subjecting the overlying crust to strong seepage action.

Through the combined effects of the above mechanisms, liquefiable soils from the entire deposit connect hydraulically and supply a large volume of pressurized water towards the ground surface. This water may escape through the crust by distributed intergranular seepage and/or localized venting, or dissipate laterally towards more permeable strata or topographic outlets. The coupled hydraulic and mechanical response of the surface crust essentially govern how the upward flow is accommodated and discharged, thereby strongly influencing the nature and severity of liquefaction manifestations at the ground surface.

3. CENTRIFUGE TESTS

3.1 OVERVIEW

Two series of three seismic centrifuge tests were performed to investigate the influence of crust characteristics on liquefaction response. Fig. 2 shows the general model configurations for the two series in prototype dimensions. Series A (Fig. 2a) employed a 12-m-deep profile comprising a loose fine-sand *critical layer* sandwiched between a denser, coarser *base sand*

and a surface *crust* that varied among tests. Series B (Fig. 2b) employed a similar but shallower, 8-m-deep profile, with an additional *intermediate layer* between the critical layer and base sand. Within each series, the geometry and properties of the liquefiable layers were kept nominally identical, while the crust type was varied. Three crusts with contrasting properties, in terms of permeability, stiffness, erodibility, and cyclic response, were examined: dense coarse sand, lightly overconsolidated silt, and heavily overconsolidated clay. All crusts were fully saturated yet classified as non-liquefiable: the sand based on its high-density state, and the silt and clay according to conventional susceptibility criteria (Boulanger and Idriss, 2006). The underlying liquefiable profiles were representative of typical VC deposits in Christchurch (Fig. 1), with grain size and liquefaction resistance generally increasing with depth. Table 1 summarizes the principal characteristics of each model test.

This paper focuses primarily on Series B (B-Sand, B-Silt and B-Clay). Selected results from Series A, previously presented in Ntritsos (2026), are included to provide supplementary evidence concerning ejecta manifestation. Data from all six tests are available through the Zenodo repository (DOI: 10.5281/zenodo.23570253).

The centrifuge tests were conducted on the 6-m-diameter beam centrifuge of ISMGEO (Istituto Sperimentale Modelli Geotecnici), Italy. The soil models were constructed inside an Equivalent Shear Beam (ESB) container, with internal dimensions of 0.730 × 0.240 × 0.337 m (length × width × depth), and tested at a nominal centrifugal acceleration of 40 g. Unless stated otherwise, all quantities in this paper are reported in prototype units according to the scaling laws provided in Garnier et al. (2007). More information on the ISMGEO centrifuge facility and ESB container can be found in Fioravante et al. (2021).

153 **3.2 MATERIALS AND MODEL CONSTRUCTION**

154 Table 2 lists the main index properties of the soils used to construct the centrifuge models.
155 The base sand in both series and the intermediate layer in Series B were prepared using Ticino
156 sand, an extensively studied, coarse-to-medium clean sand made of angular to subrounded
157 particles (e.g. Fioravante and Giretti, 2016). Ticino sand fraction TS4 ($D_{50} \approx 0.53$ mm) was
158 used for the base sand, while the slightly finer TS11 fraction ($D_{50} \approx 0.46$ mm) was used for the
159 intermediate layer. The critical layer was prepared using FF sand (FFS), a uniform, subangular,
160 very fine quartz sand ($D_{50} \approx 0.093$ mm) produced by grinding and sieving quarried rock. This
161 very fine sand was selected to ease ejecta transport to the ground surface, which can be
162 challenging in a centrifuge environment due to particle-size effects on soil-fluid interactions.
163 The static and dynamic properties of FFS are described in detail by Giretti (2010). The sand,
164 silt and clay crusts were reconstituted using TS4, TF200 and Pontida Clay (PON), respectively.
165 TF200 is a natural flour obtained by sieving Ticino sand, while PON is a well-characterized
166 kaolinitic silty clay (e.g. Hueckel and Baldi, 1990; Fioravante et al. 2021; Dodaro et al. 2025).
167 Particle-size distributions for all soils used in the tests are presented in Fig. 3.

168 Model construction was carried out in stages. First, the liquefiable layers (TS4, TS11 and
169 FFS) were dry-pluviated to the target relative densities listed in Table 1. Following the
170 pluviation, the liquefiable layers were saturated with an aqueous solution of hydroxypropyl
171 methylcellulose (HPMC) whose concentration, and hence viscosity, differed between the two
172 series. For Series A, a target kinematic viscosity of 40 cSt was selected to equate the dynamic
173 and diffusion time-scaling factors at 40 g (Garnier et al. 2007). For Series B, a lower HPMC
174 concentration was used to expedite saturation, corresponding to an estimated viscosity of 15-
175 20 cSt at the testing temperature (Adamidis and Madabhushi, 2015). This departure from strict
176 similitude was considered acceptable, given that the rate of EPP buildup during shaking was

177 unaffected while the corresponding EPP dissipation time remained substantially longer than
178 the shaking duration.

179 Saturation was initially performed by introducing the fluid from the base of the container
180 while the model was maintained under vacuum. The vacuum was slowly released once the
181 permeated volume of fluid was at least equal to the estimated pore volume. For Series B,
182 infiltration was then continued in-flight, at 40 g and atmospheric pressure, until the fluid level
183 approached the top of the container (Fig. 2b). The model was then returned to 1 g, and the
184 excess fluid above the sand surface was removed before placement of the crust. This additional
185 in-flight stage was intended to improve saturation by increasing the pore-fluid pressure, thereby
186 compressing and promoting the dissolution of entrapped air, similarly to back-pressure
187 saturation in soil element tests, and by enhancing the buoyancy-driven upward migration and
188 expulsion of remaining air bubbles. Comparison of the in-flight PPT readings before and after
189 this stage indicated improved saturation.

190 For models comprising silt or clay crusts, following the sand saturation and before
191 placement of the crust layer, a water-bentonite paste was applied on the sand-wall corners along
192 the perimeter of the container and over the exposed container walls, as shown in the
193 photographs of Fig. 4. This perimeter “bentonite gasket” was intended to limit leakage of the
194 pressurized pore fluid along the walls, a phenomenon previously observed in similar layered
195 model tests (e.g. Fiegel and Kutter, 1994), and to promote venting and sand-boil formation
196 away from the container walls. For the objectives of this study, any mechanical boundary
197 effects introduced by the gasket were considered secondary to its essential hydraulic sealing
198 function.

199 Different preparation methods were adopted for the three crusts. The sand crust was
200 reconstituted by dry pluviation and saturated together with the underlying liquefiable sands

using the procedure described above. For the silt crust, dry TF200 was mixed with deaired HPMC solution under vacuum to form a slurry. The slurry was placed on the saturated sand surface and consolidated to an average preconsolidation stress of $\sigma_p' \approx 20$ kPa. The clay crust was also prepared as a slurry but consolidated separately, using $\sigma_p' \approx 220$ kPa. After consolidation, the clay specimen was unloaded, trimmed to the target dimensions, pulled under vacuum and placed on the sand surface immediately before testing.

3.3 INSTRUMENTATION AND BASE EXCITATION

All models were instrumented with miniature accelerometers, pore pressure transducers (PPTs), and linear variable differential transformers (LVDTs), as shown in Fig. 2. All instruments were positioned on the vertical longitudinal centreplane of the container.

A ground motion recoded at the San Francisco International Airport during the 1989 Mw6.9 Loma Prieta earthquake was scaled to 0.5 g and used as the target input motion for the centrifuge tests.

4. RESULTS AND DISCUSSION

Selected results from the centrifuge tests are here presented to elucidate the influence of crust type on liquefaction response and surface manifestation. The B-Sand response is first examined in detail to illustrate key system-response mechanisms of layered VC deposits and establish a reference for subsequent comparisons. Crust effects on the subsurface liquefaction response and surface manifestations, including settlement and ejecta, are then comparatively evaluated.

4.1 REFERENCE SYSTEM RESPONSE

4.1.1 Pore-pressure and acceleration response

Fig. 5 shows acceleration and EPP time histories at the instrumented depths of the B-Sand profile. Base shaking includes a window of strong acceleration cycles between 6.3 and 12.4 s (Fig. 5a). The sand crust responds to the strong shaking with alternating positive and negative EPP spikes but negligible net buildup. This response can be explained by the initial state of the crust sand, which is well below the critical state line ($D_r \geq 80\%$, $\sigma'_{vo} \approx 0 - 20$ kPa), and by its high permeability and proximity to the free-draining ground surface. These drainage conditions allowed contractive tendencies to produce fluid outflow and densification rather than sustained EPP accumulation. In contrast, EPP builds up rapidly in the loose critical layer over the first few cycles of shaking and liquefaction is triggered ($u_e \approx \sigma'_{vo}$) with the first strong acceleration cycle at approximately 6.9 s. EPPs also develop in the deeper layers, albeit at a slower rate, and do not reach the initial effective overburden stress, σ'_{vo}. The combined effects of increased density and permeability, together with the reduced cyclic demand due to energy dissipation in the liquefied critical layer, prevented liquefaction below the critical layer.

EPP redistribution governs system response following the strong shaking. Although the intermediate layer and base sand do not liquefy, their EPPs reach approximately 40 and 50 kPa, respectively, exceeding the 28 kPa recorded in the overlying critical layer. This implies an upward hydraulic gradient and fluid flow from the deeper layers into the critical layer (mechanism 2 in Fig. 1), which is manifested by the onset of EPP dissipation immediately after the end of strong shaking (~13 s) in the deeper layers. Simultaneously, a high hydraulic gradient develops in the upper part of the deposit, with fluid flowing from the critical layer, through the crust, towards the ground surface (mechanism 3 in Fig. 1). The balance between inflow from below and outflow through the crust maintains EPP in the critical layer near σ'_{vo} for about 9 s

after end of strong shaking, followed by gradual dissipation while low-level shaking continues. The duration of elevated EPP in the critical layer, and overall evolution of EPP, reflect the coupled effects of fluid redistribution and continued soil-skeleton deformation due to shearing, both influenced by the permeability and cyclic response of adjacent layers, including the overlying crust.

These EPP responses are reflected in the recorded accelerations (Fig. 5a). Records below the critical layer generally follow the input motion pattern but exhibit amplified accelerations, with *PGA* increasing from 0.5 g at the base to 0.8 g at the bottom of the critical layer. In contrast, the acceleration immediately above the critical layer shows typical features of earthquake recordings at liquefied sites, including abrupt reduction in high-frequency content upon liquefaction triggering (~ 6.9 s), and subsequent acceleration spikes superimposed on the long-period response of the softened ground (e.g. Kramer et al. 2011; Ntritsos et al. 2021). These features reflect the overall softening and cyclic mobility behaviour associated with soil liquefaction in the critical layer. High-frequency content is partly recovered later in the record as EPP dissipates and the soil regains its stiffness.

4.1.2 Shear-strains

Fig. 6 shows average shear strain time histories for the three liquefiable layers. These strain time histories were obtained through double integration of the recorded accelerations at the top and bottom of each layer, using the methodology described by Elgamal et al. (1996). Special care was given to processing and filtering the acceleration data, as recommended by Brennan et al. (2005). The derived strain time histories show large cyclic shear strains in the critical layer during the strong shaking, in the order of 2-3%, consistent with the development of liquefaction in this layer. Moderate strains of approximately 0.5-1% continue while EPP in the critical layer remains elevated and decrease below 0.3% as EPP dissipates. Smaller strains

develop in the deeper layers which did not liquefy, reaching $\gamma_{max} \approx 0.9\%$ in the intermediate layer and $\gamma_{max} \approx 0.3\%$ in the dense base sand.

Overall, B-Sand demonstrates signature features of the VC-deposit response, including dynamic cross-layer interactions and strong diffusion effects through vertical fluid flow (e.g. Cubrinovski and Ntritsos, 2023). The dense, permeable sand crust has a particular influence on the system response by providing an efficient drainage path to the ground surface, thereby limiting sustained EPP accumulation in the upper deposit.

4.2 CRUST EFFECTS ON SUBSURFACE RESPONSE

4.2.1 Pore-pressure response

Fig. 7a compares the pore-pressure responses within each layer of the B-Sand, B-Silt, and B-Clay profiles, in terms of EPP ratio ($r_u = u_e/\sigma'_{vo}$) time-histories. Cumulative absolute velocity (CAV) time-histories of the recorded base motions are also included in Fig. 7b as a timing reference. Generally, B-Silt and B-Clay exhibit different spatial and temporal EPP distributions compared with the reference B-Sand profile.

The silt and clay crusts show sharply contrasting cyclic responses. In B-Silt, EPP rise gradually within the crust and reaches $r_u \approx 0.7$ by the end of strong shaking, indicating cyclic softening of the silt associated with substantial stiffness and strength degradation. By contrast, the OC clay crust in B-Clay develops negative EPP, with a residual $r_u \approx -0.35$. Negative EPP generation during cyclic shearing is common in heavily OC clays (OCR $\gtrsim 4$) (e.g. Vucetic and Dobry, 1986; Matasovic and Vucetic, 1995).

In the layers beneath the crust, the patterns of EPP buildup are broadly similar across all models, an exception being the critical-layer response in B-Clay. During strong shaking, r_u in this layer remains limited to approximately 0.80-0.85 and approaches unity only gradually

during subsequent void redistribution. This response is interpreted as resulting from nonuniform stress transfer across an imperfect sand-clay interface. In particular, arching of the stiff clay crust likely reduced the local initial effective stress at the PPT location relative to the theoretical overburden stress used to calculate r_u, thereby limiting the normalized EPP generated during shaking. Subsequent upward pore-fluid migration and accumulation beneath the crust progressively increased the local pore pressure, causing r_u to approach unity.

More pronounced crust effects emerge during post-liquefaction EPP redistribution and dissipation. The low permeability of the silt and clay crusts restricts upward drainage of the excess pore fluid. Consequently, upward-seeping pore fluid from the entire deposit accumulates beneath the crusts, prolonging the liquefied or near-liquefied state ($r_u \approx 1$) of the critical layers by approximately 20–30 s relative to B-Sand. Continued inflow during this phase progressively expands the soil skeleton of the critical layer, intensifying fluidization and potentially forming water-rich zones or a water film beneath the crust (e.g. Kokusho, 2003). After shaking, EPPs in B-Silt and B-Clay gradually decrease towards a quasi-uniform value throughout depth, equal to approximately 18 kPa in B-Silt and 20 kPa in B-Clay. At this stage, particle contact in the liquefied soil has been re-established and effective stress partially recovered. Subsequent dissipation of EPP is governed primarily by the effective drainage capacity of the crust, including any preferential flow paths that may develop. Similar EPP redistribution and reconsolidation patterns beneath relatively impermeable capping layers have been observed in previous physical-model studies (e.g. Fiegel and Kutter, 1994; Kokusho, 2003; Sinha et al., 2022).

The post-shaking EPP evolution within the silt and clay crusts is also noteworthy. In the silt, the high EPP dissipates slowly after the end of shaking but begins to increase again at $t \approx 1.5$ min, as upward-migrating pore fluid from the critical layer reaches the elevation of the

crust-embedded PPT. The elevated EPP persists until approximately $t \approx 30\,\mathrm{min}$, when dissipation resumes. This transient increase in EPP coincides with fluid venting and boiling at the silt surface, as discussed in subsection 4.3.2. The clay crust, which developed negative EPP during shaking, exhibits further reduction of EPP even after base shaking ceases. This continued EPP decrease is interpreted as secondary suction driven by swelling-induced deviatoric loading. Following shaking, water uptake and swelling of the basal clay imposes additional deviatoric deformation of the overlying clay at the PPT elevation; this induced a renewed dilative tendency and further negative EPP generation. The above interpretation is supported by a companion nonlinear dynamic analysis that reproduced the observed post-shaking trend.

In addition to the swelling-induced deviatoric deformation, local bending of the clay crust may contribute to the accelerated suction development after $t \approx 1.7\,\mathrm{min}$ by inducing an undrained extensional-unloading response. B-Clay uniquely combines a stiff, coherent crust with liquefied and severely loosened sand beneath it. Small pre-existing irregularities at the sand-clay interface can be amplified into markedly nonuniform contact during liquefaction and void redistribution, as the stiff clay bridges across the deforming sand surface. As the accumulated fluid pressure beneath the crust subsequently dissipates, localized loss of support may cause the crust to sag. This downward sagging and bending would place the lower part of the crust in tension and could further increase suction at the PPT elevation. From approximately $t \approx 6\,\mathrm{min}$ onward, hydraulic redistribution and equalization dominate, and the negative EPP gradually dissipates toward zero.

337 **4.2.2 Shear strains and post-liquefaction ground response**

338 Fig. 8 compares the average shear-strain time-histories and cumulative shear-strain time-
339 histories in the critical layers of the three models. Cumulative shear-strain was calculated by
340 summing the absolute shear-strain increments:

341 $$\Gamma(t_n) = \sum_{i=2}^{n} |\gamma_i - \gamma_{i-1}| \quad (1)$$

342 where t_n denotes the time corresponding to n^{th} the data point.

343 In all models, the largest strains and highest rates of strain accumulation occur during the
344 high-acceleration interval between 6.3 and 12.4 s. Peak shear strains range from 2.5% in B-
345 Sand to 3.4% in B-Silt. After strong shaking, strain accumulation in B-Clay continues at a
346 progressively lower rate, as the input motion also weakens with time (Fig. 8c). B-Sand follows
347 a similar trend until approximately $t \approx 16$ s, after which strain accumulation significantly
348 diminishes as EPP dissipates and the critical layer regains stiffness and strength. In B-Silt, the
349 rate of strain accumulation decreases earlier, near the end of strong shaking, despite the critical
350 layer retaining elevated EPP, similar to B-Clay (Fig. 7a). Thus, although both critical layers
351 remain highly softened, moderate strain accumulation persists in B-Clay but is strongly
352 suppressed in B-Silt. This difference in the strain response may indicate reduced external
353 demand or pronounced seismic attenuation effects within the B-Silt profile (e.g. Cubrinovski
354 and Ntritsos, 2023). The slightly weaker base motion in B-Silt after $t \approx 15$ s (Fig. 8c) can
355 explain only a small part of this difference.

356 To investigate this discrepancy, Fig. 9a compares the ratios of the elastic response spectra
357 at the top of the critical layer to those at the model base. To focus upon the part of the response
358 where cumulative strains differ most, the response spectral ratios (*RSRs*) in Fig. 9a were
359 calculated considering only the spectral response after $t = 16$ s. The corresponding base-motion

spectra are shown in Fig. 9b. B-Clay exhibits *RSR* characteristics typical of liquefied profiles (e.g. Kramer et al. 2011, Bouckovalas et al. 2016), with attenuation at periods up to approximately 0.7 s, followed by amplification at longer periods. B-Sand shows a broadly similar response, but with several localized amplifications between approximately 0.3 and 0.7 s, reflecting the partial recovery of the critical-layer stiffness during this later excitation stage. By contrast, B-Silt exhibits substantially stronger and broader attenuation up to about 2 s period. Indicatively, *RSRs* are only 0.37, 0.24 and 0.16 at periods T = 0.27, 0.45 and 0.6 s, respectively, which correspond to peaks in the base-motion spectrum (Fig. 9b). This stronger attenuation in B-Silt is consistent with the reduced strain accumulation observed in its critical layer (Fig. 8b).

Companion linear viscoelastic analyses, not presented herein, indicate that the stronger attenuation in B-Silt, relative to B-Clay, cannot be explained by their differences in the sand-crust impedance contrast or by greater damping in the silt crust. Reproducing the B-Silt attenuation in these analyses requires a substantial reduction in the critical-layer shear-wave velocity, consistent with more extensive fluidization than in B-Clay. In B-Clay, the high-stiffness contrast across the sand-clay interface may promote localization of soil-skeleton disturbance immediately beneath the crust, limiting its extent within the deeper part of the critical layer.

4.3 CRUST EFFECTS ON SURFACE MANIFESTATION

4.3.1 Settlement

Fig. 10a compares the surface settlement responses of the three models, with settlement in each test calculated as the average of the two surface LVDT measurements. The timing of key stages of shaking is also indicated in this figure. Both the magnitude and temporal evolution of settlement appear to depend strongly on the crust type.

B-Sand exhibits substantial co-seismic settlement: approximately 50% of the final settlement develops by the end of strong shaking and 94% by the time base shaking ceases. This early settlement provides further evidence of partial drainage through the permeable crust during shaking, consistent with the indications of the pore-pressure measurements (Fig. 5). Most of the final settlement of 6.4 cm can be attributed to post-liquefaction sedimentation and reconsolidation of the critical layer, with negligible contribution from the dense crust itself.

B-Clay develops a mean recorded settlement similar to that of B-Sand during strong shaking, despite the clay crust would be expected to prevent fluid drainage and preserve constant model volume (i.e. zero settlement) in the short term. This early settlement indicates possible localized drainage through cracks or fissures in the clay and gaps at the bentonite-wall or clay-bentonite interfaces, which are potentially enlarged during shaking. Part of the recorded mean settlement may also reflect spatially nonuniform movement of the crust, with local sagging at the LVDT locations offset by heave elsewhere. Under the nonuniform support conditions discussed in subsection 4.2.1, horizontal inertia acting on the bridging crust may induce local bending or rigid-body rocking, resulting in both permanent and reversible differential vertical movements. The large opposite-phase fluctuations of the two LVDT records of B-Clay, shown in Fig. 10b, provide evidence of nonuniform crust movement consistent with this mechanism.

After strong shaking, surface settlement in B-Clay accumulates much more slowly than in B-Sand. The coherent, low-permeability crust temporarily decouples surface movement from sedimentation of the underlying sand, as expelled pore fluid accumulates beneath or enters the crust rather than being discharged immediately. Pore-fluid absorption and the associated swelling of the OC clay may further offset part of the underlying sand settlement. Subsequent surface settlement is governed by coupled sand reconsolidation and drainage through the crust

and any preferential flow paths. Reconsolidation is essentially complete within approximately 2 h, producing a final settlement of about 5.9 cm, slightly less than that in B-Sand.

B-Silt exhibits the largest settlement of the three models, reaching approximately 11 cm at the end of reconsolidation. Approximately 94% of this settlement develops during shaking, indicating localized drainage and coupled deformation of the critical layer and silt crust. Initial restriction of upward drainage causes pore fluid to accumulate beneath the crust, expanding and severely fluidizing the critical layer. Meanwhile, the combined effects of cyclic and seepage-induced softening of the silt cause strong crust disturbance and an increase in its effective hydraulic conductivity, possibly involving channelized drainage paths. The softened silt loses its ability to bridge over the subsiding sand; instead, it deforms with the underlying layer and may itself undergo particle rearrangement while transmitting upward-flow, resulting in rapid net surface settlements. The large co-seismic settlement of B-Silt is therefore interpreted as the combined consequence of extensive fluidization of the critical layer, localized discharge and deformation of the softened silt crust.

The comparative analysis of the settlement responses of the three models suggests that crust characteristics may strongly influence liquefaction-induced ground deformations and associated damage. The silt crust combines sufficient hydraulic resistance to intensify void redistribution effects with insufficient mechanical resistance to prevent subsequent loss of crust integrity. The result was severe fluidization of the critical layer, breakdown of the silt structure and efficient transmission of subsurface deformation to the ground surface. By contrast, the OC clay largely retained its stiffness and structural integrity and partly decoupled surface movement from sedimentation of the underlying sand. In field settings, where liquefaction effects and associated deformations can be highly nonuniform, such contrasting crust responses may produce markedly different patterns of differential ground movement and damage.

In current engineering practice, settlement of liquefiable deposits is often estimated without considering the response and effects of capping non-liquefiable layers. Furthermore, these settlement estimates generally rely on empirical relationships between post-liquefaction volumetric strain and maximum cyclic shear strain, with the latter serving as a proxy for the degree of soil-skeleton disturbance. The lack of correspondence between the shear strains in Fig. 8 and settlements in Fig. 10 challenges this $\gamma_{max} - \varepsilon_{vol}$ link for layered deposits undergoing void redistribution. The idealized sequence underlying these relationships – undrained cyclic loading followed by free drainage – does not capture partial drainage during shaking, interlayer pore-fluid redistribution and fluidization effects, or localized discharge. The results of this study suggest that undrained cyclic shear strain alone may not fully characterize settlement potential in layered deposits, for which the actual degree and spatial extent of skeleton disturbance and the hydraulic and mechanical response of the crust may also be important.

4.3.2 Ejecta

Ejecta manifestation characteristics also varied with crust type.

Models with a coarse TS4 sand crust did not produce surface ejecta in any of the tests performed. This is consistent with previous experimental evidence indicating that a finer-grained, lower-permeability layer capping the liquefiable zone and allowing pressure to accumulate beneath the crust is generally required for ejecta formation (e.g. Scott and Zuckerman, 1973; Fiegel and Kutter, 1994; Brennan and Madabhushi, 2005). In the sand-crust models, EPP is instead rapidly relieved through broadly distributed intergranular seepage, with little pore pressure development or disturbance within the crust (Fig. 5b). The resulting hydraulic gradients acting within the crust are therefore insufficient to erode the coarse sand particles and create ejecta pathways to the ground surface.

Models with intact OC clay crusts also did not produce ejecta or any visible surface cracks. In such stiff and coherent crusts, ejecta most likely occurs by localized venting through cracks or fissures, rather than by progressive erosion of the crust soil particles as in non-plastic soils. Such preferential pathways to the ground surface may be pre-existing (e.g. desiccation cracks, animal burrows) or develop through hydraulic fracturing or cyclic ground deformation (Obermeier et al., 2005).

To explore the effect of such openings, B-Clay was retested after four 3-mm-diameter holes were drilled approximately through the full crust thickness. At each LVDT's longitudinal position (Fig. 2b), one hole was placed approximately halfway between the LVDT and each longitudinal sidewall. Sand (FFS) ejecta emerged from one of these holes approximately 4 min after shaking. A close-up photograph of the ejecta taken after removal of the supernatant fluid is shown in Fig. 11a. Apart from the ejecta, the second test produced pore-pressure and settlement records similar to those obtained during the first test on the intact model, indicating that stopping the centrifuge to drill the holes, restarting and re-shaking the model did not materially alter its overall response.

Ejecta was consistently observed in the silt-crust models. In these tests, surface boiling began within approximately 3 min after shaking and coincided with a characteristic transient increase in EPP recorded by the crust-embedded PPTs, as indicated in Fig. 12. In B-Silt, video recordings showed fluid venting and suspension of silt particles, although sand ejecta was minor and confined to one transverse edge of the model. A-Silt, which had a thicker critical layer (4.8 m vs. 2.0 m in B-Silt) and a higher-viscosity fluid (40 cSt vs. 15-20 cSt in B-Silt), produced more severe ejecta, with sand boils at three distinct locations. The two largest sand boils occurred in the central part of the model near the longitudinal side walls, where there is likely a concentration of seepage paths due to the bentonite gasket (Fig. 4) forcing flow inwards

480 within the soil mass. A third smaller sand boil formed closer to the longitudinal centreline. Fig.
481 11b shows a top view of one of the larger ejecta features in A-Silt. The greater ejecta severity
482 in A-Silt, relative to B-Silt, may reflect the combined effects of: (a) the increased thickness of
483 liquefaction and (b) the slower settling velocity of suspended particles (due to the more viscous
484 pore fluid) – a factor associated with sand-boil development by Scott and Zuckerman (1973).

485 The silt crust combines hydraulic and mechanical properties conductive to the formation
486 of sediment ejecta. Its low permeability promotes pressure accumulation and prolonged state
487 of liquefaction beneath the crust, while its low cyclic resistance allows high EPP generation
488 and weakening of the soil skeleton. Its fine grain size and weak interparticle bonding also
489 provide relatively low resistance to erosion. Together, these characteristics facilitate
490 progressive erosion and the formation of localized channels through which pore fluid and
491 suspended sediment can reach the ground surface.

492 ## 5. CONCLUSIONS

493 Seismic centrifuge tests were performed to investigate how the hydromechanical
494 characteristics of a non-liquefiable crust influence the response of layered liquefiable deposits.
495 The experiments involved two vertically continuous liquefiable profiles, each overlain by three
496 contrasting crust types: dense coarse sand, lightly overconsolidated silt, and heavily
497 overconsolidated clay. The principal findings are summarized below.

498 1. Vertically continuous deposits are characterized by thick and continuous liquefiable layers
499 which, under strong seismic shaking, connect hydraulically and supply a large volume of
500 pressurized water towards the ground surface. The hydromechanical properties of the non-
501 liquefiable surface crust govern how this inflow is accommodated and discharged, thereby
502 directly influencing the nature and severity of liquefaction damage.

2. Crust permeability controls pore-fluid discharge and redistribution. In coarse sand-crust models, excess pore pressure is rapidly relieved through broadly distributed intergranular seepage, with little disturbance within the crust. Substantial drainage takes place during shaking, reducing the severity of liquefaction in the critical layer and consequent ejecta potential, while enabling early co-seismic settlement. Conversely, the low-permeability silt and clay crusts restrict upward drainage and promote pore-fluid accumulation beneath them. Combined with sustained upward flow from deeper layers, this creates conditions for severe fluidization of the critical layer and increased ejecta potential. Full development of surface settlement can be delayed, with its timing governed primarily by the effective drainage capacity of the crust, including any preferential flow paths that may develop during or after shaking.
3. Stiffness and structural integrity of the crust influence how subsurface deformation is transmitted to the ground surface and may also affect the spatial extent of subsurface liquefaction effects. The softened silt deforms with the subsiding sand and potentially contributes additional settlement through its own skeleton disturbance. The stiff, coherent clay, instead, can bridge across the deforming sand surface, partially decoupling surface movement from underlying sand sedimentation, and hence mitigating ground surface distortion. Furthermore, the high-stiffness contrast across the sand-clay interface appears to promote localization of soil-skeleton disturbance immediately beneath the crust, limiting its extent within the deeper sand.
4. Crust resistance to erosion or fracture controls the development of ejecta pathways. Ejecta occurred consistently in the silt-crust models and also emerged though an artificially introduced opening in a clay-crust test. Intact clay and sand crusts produced no surface ejecta. These observations highlight the importance of both crust resistance and pathway availability: pressure accumulation beneath a low-permeability crust does not alone ensure

surface ejecta. The particle weight (size) and interparticle bonding are important in determining the erosion resistance of the crust.

5. The cyclic response of the crust can modify the properties discussed above and the overall hydromechanical behaviour of the crust. The silt developed high positive EPP and underwent substantial cyclic softening, making it more susceptible to deformation and erosion under continued upward seepage. By contrast, the heavily OC clay exhibited dilative tendencies with negative EPP development and largely retained its stiffness and structural integrity. Subsequent pore-fluid uptake and swelling could partly accommodate fluid expelled from the underlying sand and offset its contribution to surface settlement. Crusts nominally classified as non-liquefiable can therefore exhibit markedly different cyclic responses, with contrasting consequences for liquefaction-induced deformation and ejecta.

Together, these findings demonstrate that contrasting crust properties can produce markedly different patterns of pore-pressure redistribution, settlement and ejecta, with important consequences for differential ground movement and liquefaction-related damage. Assessment of liquefaction consequences would therefore substantially benefit from explicit consideration of the coupled hydraulic and mechanical response of the crust.

To this end, further research, including tests on unsaturated crusts, is needed to better understand the contributions of individual crust properties and quantify their combined effects on deposit response and surface damage. For centrifuge investigations of ejecta, using sufficiently fine sand in the critical layer can facilitate sediment transport, while pore-fluid viscosity should be selected considering its effects on both seepage and particle-settling rates. Appropriate perimeter sealing, for example using a bentonite gasket, is also recommended to limit unintended drainage along container walls.

ACKNOWLEDGEMENTS

I would like to thank the ISMGEO staff for their hospitality and contributions to the centrifuge experiments. Special thanks to Mr. Sergio Airoldi (ISMGEO) for overseeing the experimental programme and Prof. Vincenzo Fioravante (University of Ferrara) for advising on the experimental design. Discussions with Dr. Mark Stringer and Prof. Misko Cubrinovski (University of Canterbury), Dr. Dan Wilson and Prof. Katerina Ziotopoulou (UC Davis), and Prof. Carlo G. Lai (University of Pavia) helped resolve experimental challenges and are gratefully acknowledged. Review comments from Prof. Misko Cubrinovski on a draft of this manuscript are also appreciated.

This research was conducted within the LiqproofHouses project, which has received funding from the European Union's Horizon Europe research and innovation programme under Marie Sklodowska-Curie grant agreement No. 101206235.

REFERENCES

Adamidis, O., Madabhushi, S.P.G. (2015). Use of viscous pore fluids in dynamic centrifuge modelling. *International Journal of Physical Modelling in Geotechnics*, 15(3), 141-149.

Bassal, P.C., Boulanger, R.W., DeJong, J.T. (2022). System response of an interlayered deposit with spatially distributed ground deformations in the Chi-Chi earthquake. *Journal of Geotechnical and Geoenvironmental Engineering*, 148(10), 05022004.

Bouckovalas, G., Dakoulas, P. (2007). Liquefaction performance of shallow foundations in presence of a soil crust. *In: Pitilakis, K.D. (Ed.), Earthquake Geotechnical Engineering; Geotechnical, Geological and Earthquake Engineering, vol 6.*, pp. 245-276, Springer.

573 Bouckovalas, G.D., Tsiapas, Y.Z., Theocharis, A.I., Chaloulos, Y.K. (2016). Ground response
574 at liquefied sites: seismic isolation or amplification? *Soil Dynamics and Earthquake*
575 *Engineering*, 91, 329-339.

576 Boulanger, R.W., Idriss, I.M. (2006). Liquefaction susceptibility criteria for silts and clays.
577 *Journal of Geotechnical and Geoenvironmental Engineering*, 132(11), 1413-1426.

578 Brennan, A.J., Madabhushi, S.P.G. (2005). Liquefaction and drainage in stratified soil. *Journal*
579 *of Geotechnical and Geoenvironmental Engineering*, 131(7), 876-885.

580 Brennan, A.J., Thusyanthan, N.I., Madabhushi, S.P.G. (2005). Evaluation of shear modulus
581 and damping in dynamic centrifuge tests. *Journal of Geotechnical and Geoenvironmental*
582 *Engineering*, 131(12), 1488-1497.

583 Cubrinovski, M., Ntritsos, N. (2023). 8th Ishihara lecture: Holistic evaluation of liquefaction
584 response. *Soil Dynamics and Earthquake Engineering*, 168, 107777.

585 Cubrinovski, M., Rhodes, A., Ntritsos, N., van Ballegooy, S. (2019). System response of
586 liquefiable deposits. *Soil Dynamics and Earthquake Engineering*, 124, 212-229.

587 Dhakal, R., Ntritsos, N., Cubrinovski, M. (2026). Evaluation of liquefaction ejecta potential
588 from case histories and insights from nonlinear dynamic analyses. *Journal of Geotechnical*
589 *and Geoenvironmental Engineering*, 152(1), 04025174.

590 Dodaro, E., Giretti, D., Pirone, M., Ventini, R., Fioravante, V., Gottardi, G., Mancuso, C.
591 (2025). Insights into the hydromechanical behavior of a river embankment through physical
592 and numerical modeling. *Journal of Geotechnical and Geoenvironmental Engineering*,
593 151(8), 04025075.

594 Elgamal, A.-W., Zeghal, M., Taboada, V., Dobry, R. (1996). Analysis of site liquefaction and
595 lateral spreading using centrifuge testing records. *Soils and Foundations*, 36(2), 111-121.

596 Fiegel, G.L., Kutter, B.L. (1994). Liquefaction mechanism for layered soils. *Journal of*
597 *Geotechnical Engineering*, 120(4), 737-755.

598 Fioravante, V., Giretti, D. (2016). Unidirectional cyclic resistance of Ticino and Toyoura sands
599 from centrifuge cone penetration tests. *Acta Geotechnica*, 11(4), 953-968.

600 Fioravante, V., Giretti, D., Airoldi, S., Moglie, J. (2021). Effects of seismic input, fine crust
601 and existing structure on liquefaction from centrifuge model tests. *Bulletin of Earthquake*
602 *Engineering*, 19(10), 3807-3833.

603 Garnier, J., Gaudin, C., Springman, S.M., Culligan, P.J., Goodings, D., Konig, D., Kutter, B.,
604 Phillips, R., Randolph, M.F., Thorel, L. (2007). Catalogue of scaling laws and similitude
605 questions in geotechnical centrifuge modelling. *International Journal of Physical*
606 *Modelling in Geotechnics*, 7(3), 1-23.

607 Giretti, D. (2010). Modelling of piled raft foundations in sand. Ph.D. thesis, University of
608 Ferrara, Ferrara, Italy.

609 Hueckel, T., Baldi, G. (1990). Thermoplasticity of saturated clays: experimental constitutive
610 study. *Journal of Geotechnical Engineering*, 116(12), 1778-1796.

611 Hutabarat, D., Bray, J.D. (2022). Estimating the severity of liquefaction ejecta using the cone
612 penetration test. *Journal of Geotechnical and Geoenvironmental Engineering*, 148(3),
613 04021195.

614 Ishihara, K. (1985). Stability of natural deposits during earthquakes. *In: Proceedings of the*
615 *11th International Conference on Soil Mechanics and Foundation Engineering*, 12-16
616 August 1985, San Francisco, CA, Vol. 1, pp. 321-376. A.A. Balkema.

617 Kokusho, T. (2003). Current state of research on flow failure considering void redistribution
618 in liquefied deposits. *Soil Dynamics and Earthquake Engineering*, 23(7), 585-603.

Kramer, S.L., Hartvigsen, A.J., Sideras, S.S., Ozener, P.T. (2011). Site response modeling in liquefiable soil deposits. *In: Proceedings of the 4th IASPEI/IAEE International Symposium on the Effects of Surface Geology on Seismic Motion*, 23-26 August 2011, University of California, Santa Barbara, CA.

Matasović, N., Vucetic, M. (1995). Generalized cyclic-degradation-pore-pressure generation model for clays. *Journal of Geotechnical Engineering*, 121(1), 33-42.

Naesgaard, E., Byrne, P.M., Ven Huizen, G. (1998). Behaviour of light structures founded on soil 'crust' over liquefied ground. *In: Dakoulas, P., Yegian, M., Holtz, R.D. (Eds.), Geotechnical Earthquake Engineering and Soil Dynamics III*, *Geotechnical Special Publication No. 75, Vol. 1,* pp. 422-433, ASCE.

Ntritsos, N., Cubrinovski, M., Bradley, B.A. (2021). Challenges in the definition of input motions for forensic ground-response analysis in the near-source region. *Earthquake Spectra*, 37(4), 2562-2595.

Ntritsos, N. (2026). Crust influence on liquefaction response and ejecta manifestation. *In: Proceedings of the 5th International Conference on Performance Based Design on Earthquake Geotechnical Engineering*, 4–6 November 2026, Puerto Varas, Chile.

Obermeier, S.F., Olson, S.M., Green, R.A. (2005). Field occurrences of liquefaction-induced features: a primer for engineering geologic analysis of paleoseismic shaking. *Engineering Geology*, 76(3-4), 209-234.

Scott, R.F., Zuckerman, K.A. (1973). Sandblows and liquefaction. *In: The Great Alaska Earthquake of 1964: Engineering*, pp. 179-189, National Academy of Sciences.

Sinha, S.K., Ziotopoulou, K., Kutter, B.L. (2022). Centrifuge model tests of liquefaction-induced downdrag on piles in uniform liquefiable deposits. *Journal of Geotechnical and Geoenvironmental Engineering*, 148(7), 04022048.

Vucetic, M., Dobry, R. (1986). Cyclic degradation of normally and overconsolidated clays under simple shear loading conditions. Report No. CE-86-01, Department of Civil Engineering, Rensselaer Polytechnic Institute, Troy, NY.

Yoshimi, Y., Kuwabara, F. (1973). Effect of subsurface liquefaction on the strength of surface soil. *Soils and Foundations*, 13(2), 67-81.

TABLES

Table 1. Summary of centrifuge model configurations and soil state parameters

Model	Crust						Critical layer				Intermediate layer				Base sand			
	MC[1]	γ_{sat}[2] (kN/m^3)	D_r[3] (%)	σ_p[4] (kPa)	w[5] (%)	h[6] (m)	MC	γ_{sat} (kN/m^3)	D_r (%)	h (m)	MC	γ_{sat} (kN/m^3)	D_r (%)	h (m)	MC	γ_{sat} (kN/m^3)	D_r (%)	h (m)
A-Sand	TS4	19.8	80	—	—	2.0												
A-Silt	TF200	19.6	—	20	29	2.0	FFS	17.7	30	4.8	—	—	—	—	TS4	19.4	60	5.2
A-Clay	PON	21.0	—	400	19	2.0												
B-Sand	TS4	19.8	80	—	—	2.0												
B-Silt	TF200	19.1	—	20	32	2.0	FFS	17.7	30	2.0	TS11	18.5	30	2.0	TS4	19.4	60	2.0
B-Clay	PON	20.6	—	220	21	2.0												

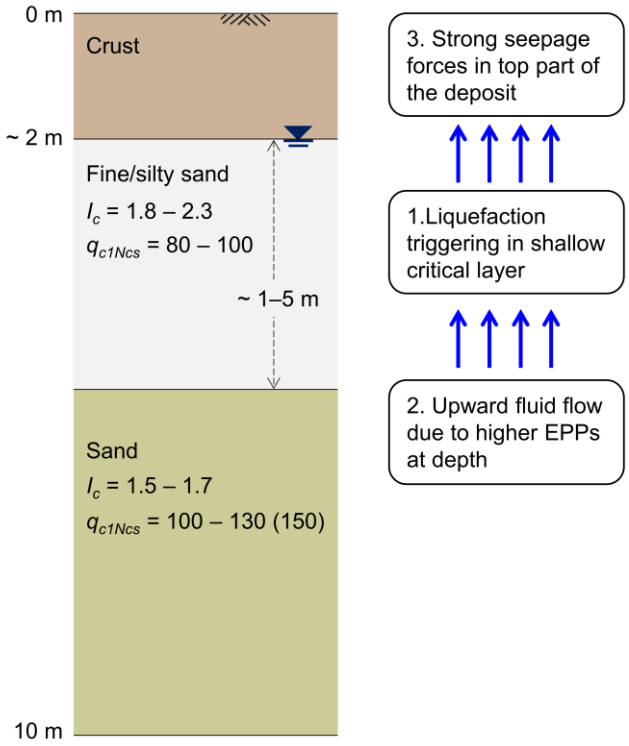
Notes: [1] MC = material code; [2] γ_{sat} = saturated unit weight; [3] D_r = relative density determined during model reconstitution; [4] σ_p = average preconsolidation stress; [5] w = gravimetric water content; [6] h = layer thickness

Table 2. Index properties of the soils used in the centrifuge models

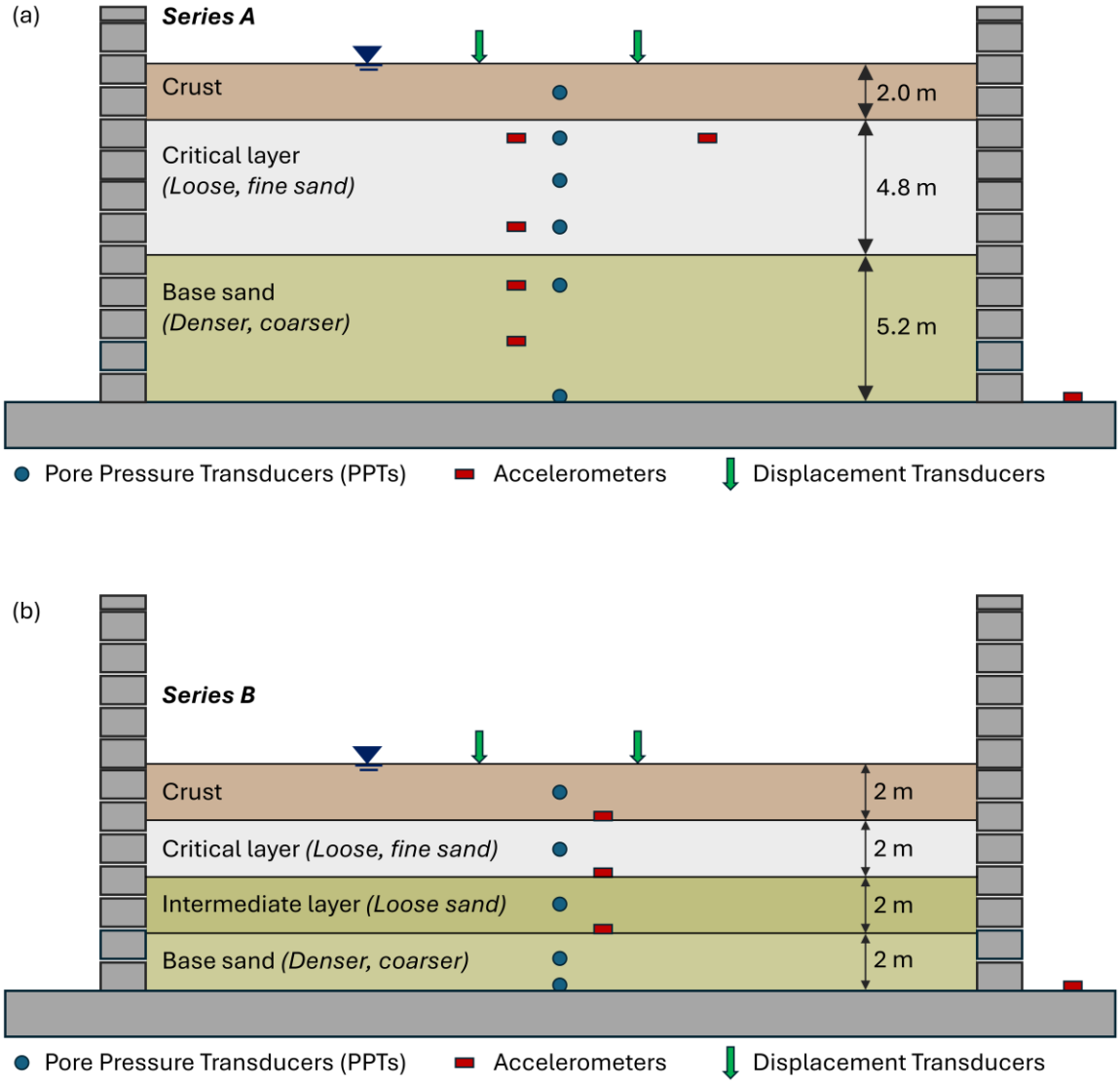
Property	TS4	TS11	FFS	TF200	PON
Specific gravity, G_s	2.68	2.70	2.66	2.81	2.74
Median grain size, D_{50} (mm)	0.53	0.46	0.093	0.022	0.005
Minimum void ratio, e_{min}	0.576	0.634	0.702	—	—
Maximum void ratio, e_{max}	0.926	1.026	1.198	—	—
Liquid limit, LL (%)	—	—	—	31	24
Plasticity index, PI (%)	—	—	—	7	11

FIGURES

Figure 1. Typical soil profile characteristics (left) and liquefaction response scenario (right) for vertically continuous deposits.

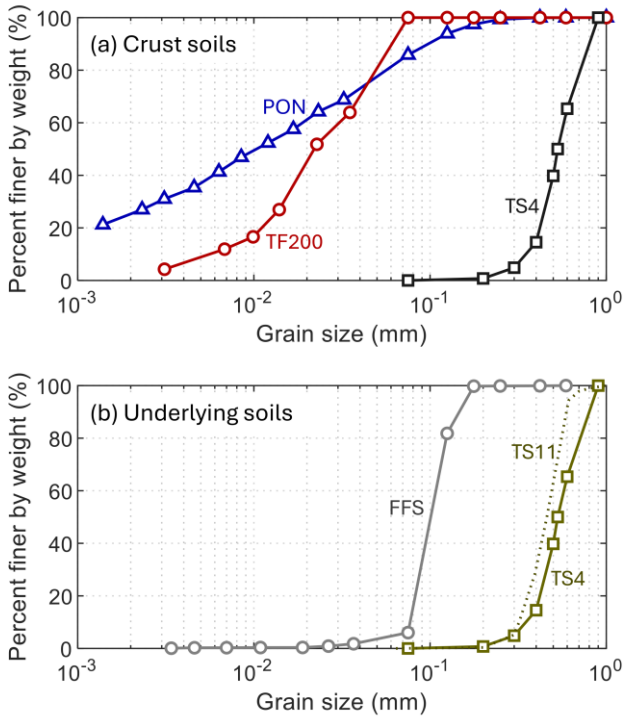


663 Figure 2. Schematic cross-sections of the centrifuge models: (a) Series A; (b) Series B.
664 Dimensions are given in prototype scale.



665
666

667 Figure 3. Grain size distribution curves of the soils used in the centrifuge models: (a) crust
668 soils; (b) underlying soils.

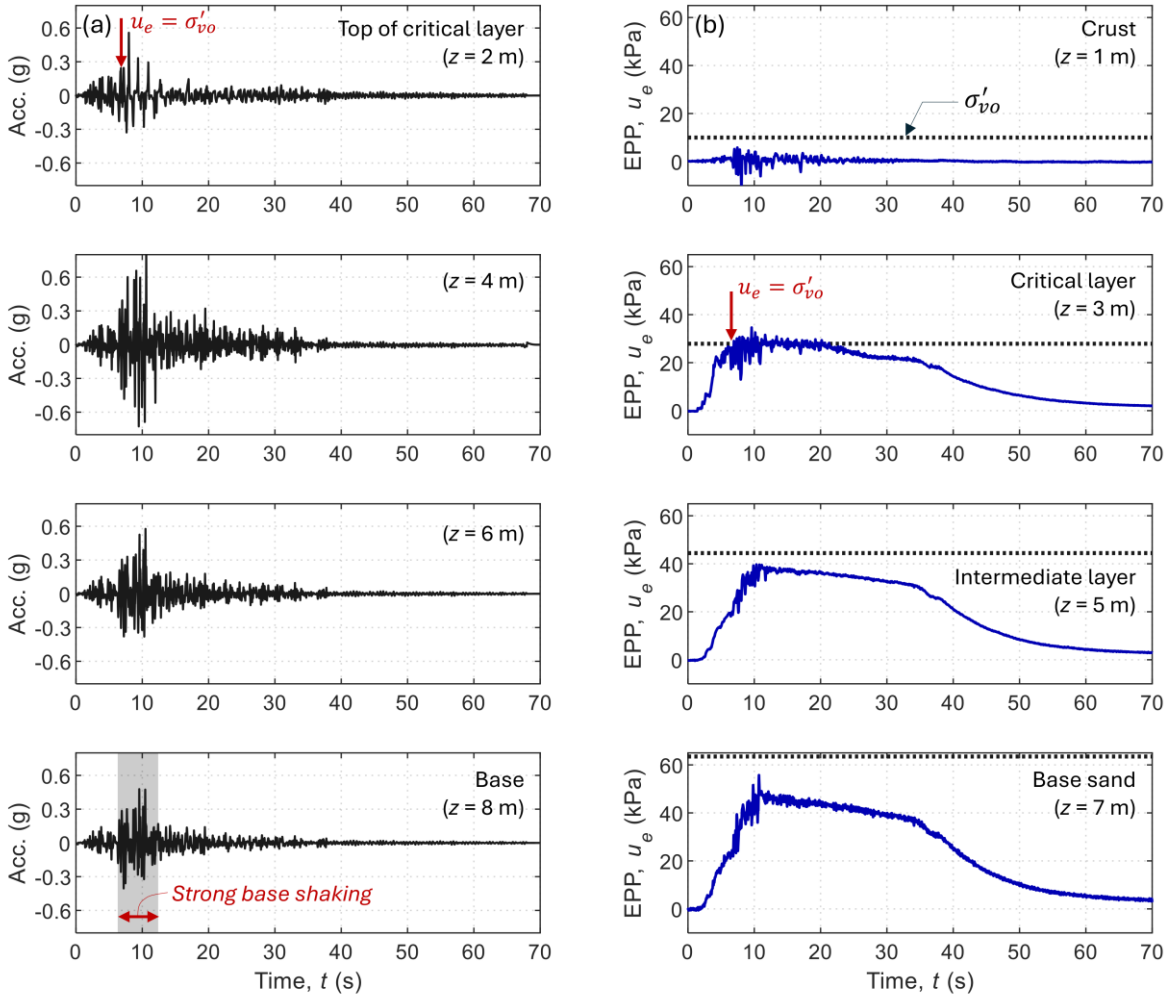


669
670

Figure 4. Photographs of the perimeter bentonite gasket, applied after sand saturation and before crust placement to limit fluid and ejecta leakage along the container walls.



675 Figure 5. Acceleration and excess pore pressure time histories recorded at the instrumented
676 depths of the B-Sand profile: (a) accelerations; (b) excess pore pressures.



677
678

Figure 6. Average shear strain time histories for the liquefiable layers of B-Sand, derived from double integration of the acceleration records at the layer boundaries.

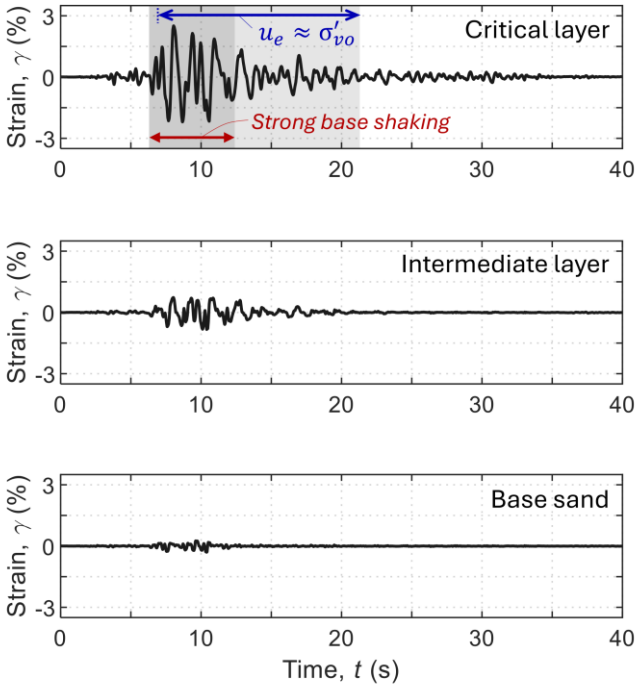


Figure 7. Comparison of excess pore pressure responses in B-Sand (black), B-Silt (red) and B-Clay (blue): (a) excess pore pressure ratio time histories within each layer; (b) cumulative absolute velocity of the base motion. Time axes are discontinuous.

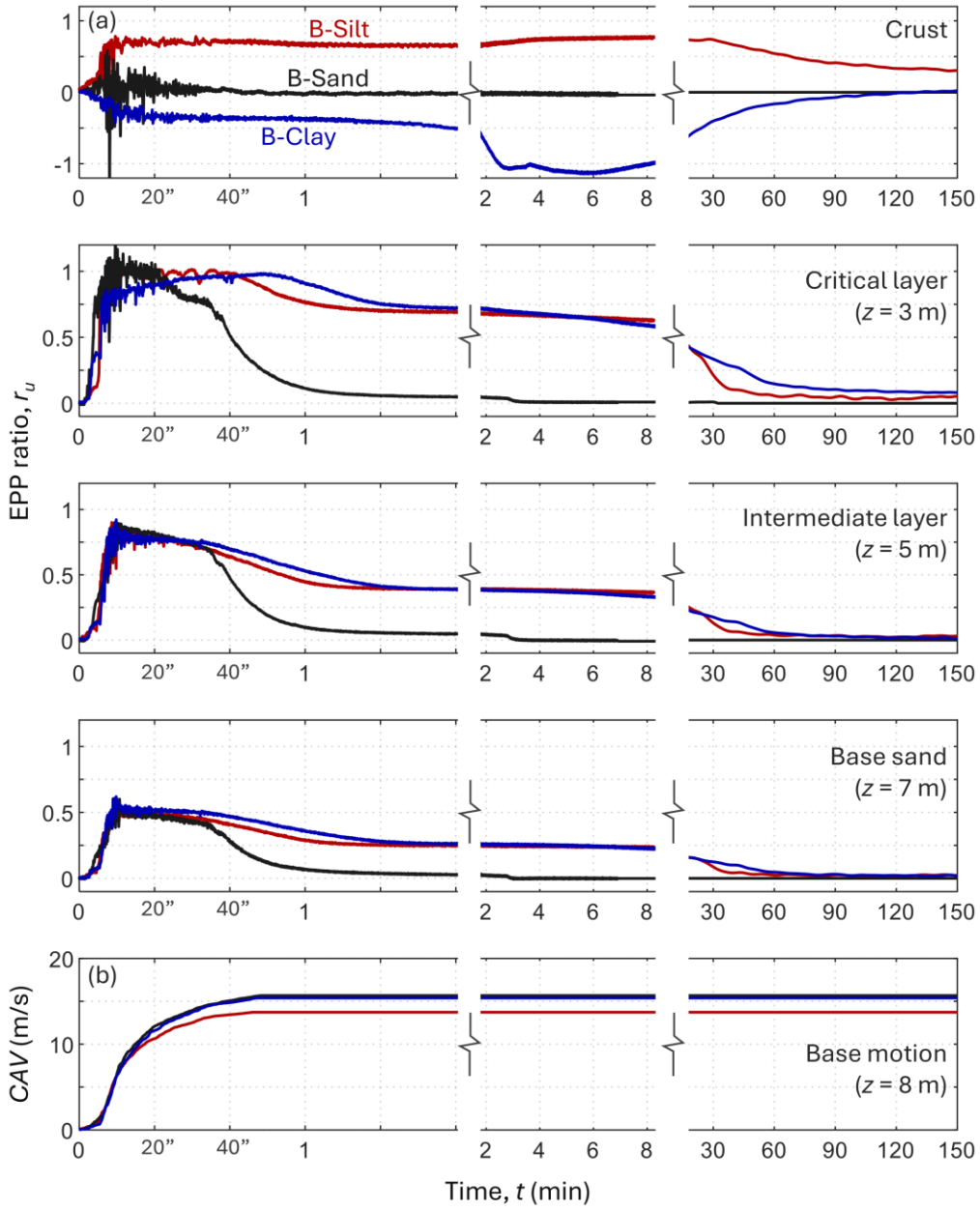


Figure 8. Comparison of the critical-layer shear strain responses in B-Sand (black), B-Silt (red) and B-Clay (blue): (a) average shear strain; (b) cumulative shear strain, calculated by summing the absolute increments of the average shear strain; (c) cumulative absolute velocity of the base motion.

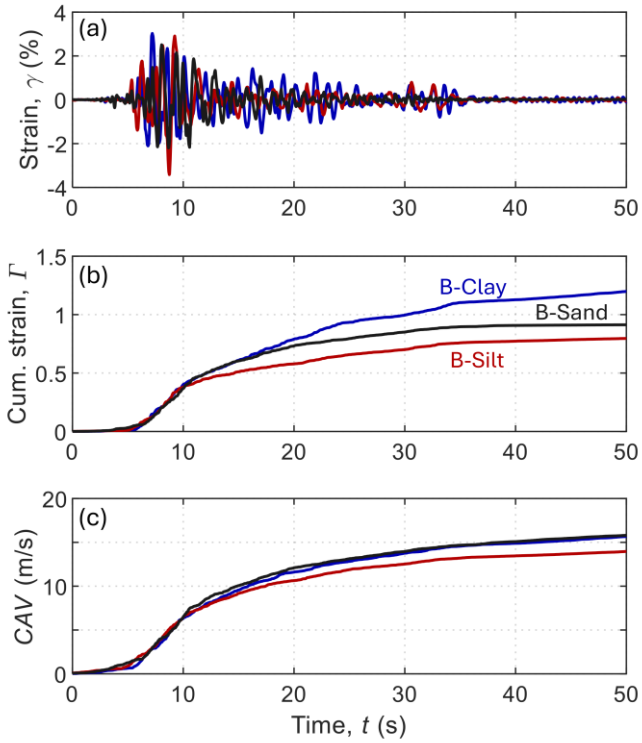


Figure 9. Ground motion attenuation and amplification effects in B-Sand (black), B-Silt (red) and B-Clay (blue) after t = 16 s: (a) ratios of the elastic response spectra (5% damping) at the top of the critical layer to those at the model base; (b) corresponding base-motion response spectra.

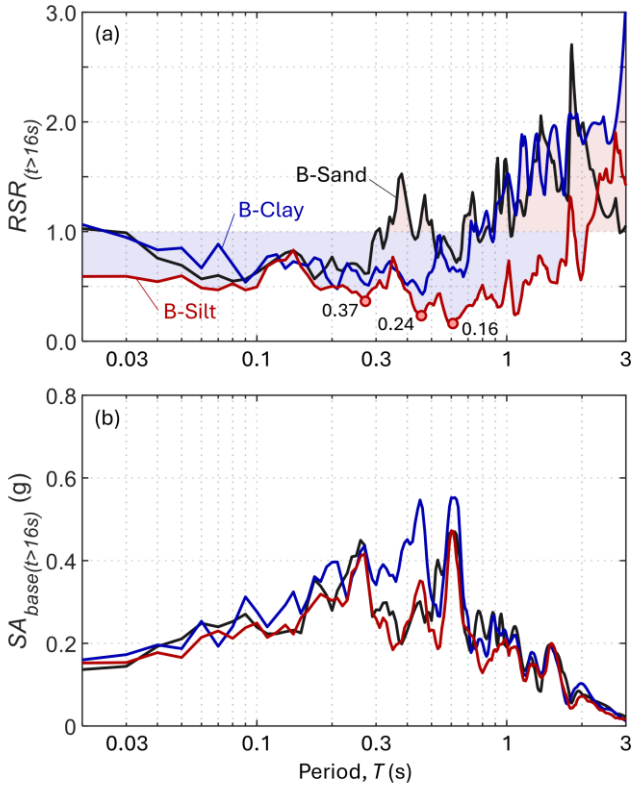
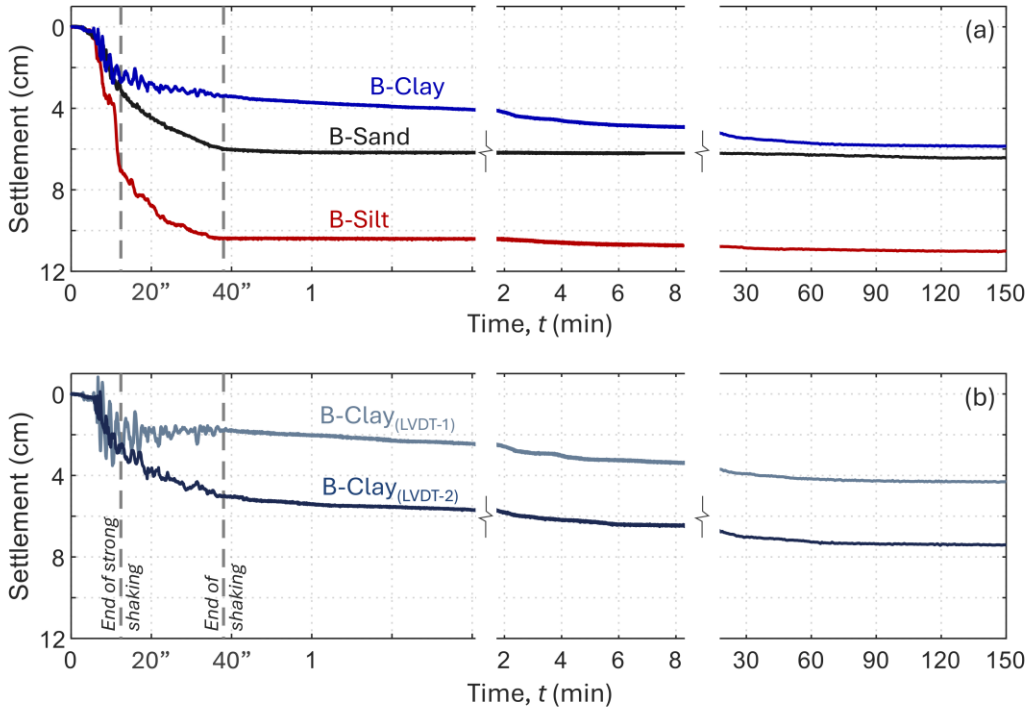
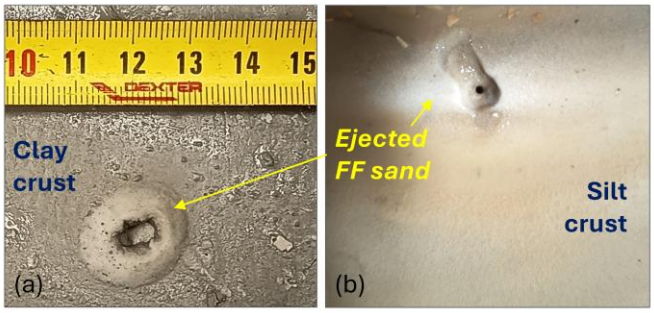


Figure 10. Surface settlement time histories for B-Sand (black), B-Silt (red) and B-Clay (blue): (a) average settlements calculated from the two surface LVDT measurements; (b) opposite-phase fluctuations of the individual LVDT records in B-Clay, consistent with rigid-body rocking of the clay crust. Time axes are discontinuous.

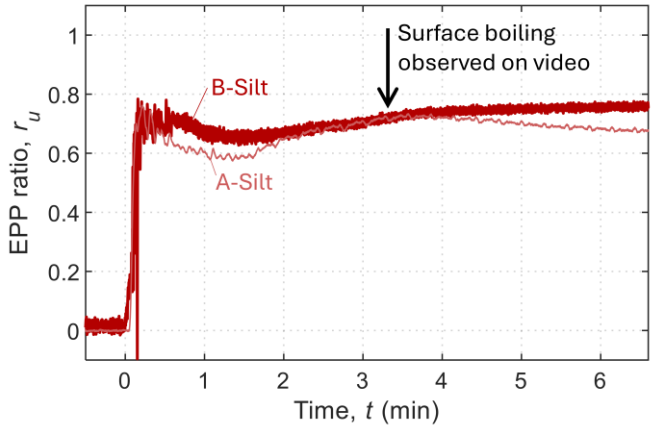


706 Figure 11. Post-test top-view photographs of FF sand ejecta: (a) ejecta emerged from an
707 artificially introduced opening in B-Clay; (b) ejecta in A-Silt. A significant portion of the A-
708 Silt ejecta is not visible as it was dispersed within ponded surface fluid during the test.



709
710

711 Figure 12. Excess pore pressure ratio time histories recorded by the crust-embedded PPTs in
712 A-Silt and B-Silt, and timing of surface boiling identified from video recordings of each test.



713